Response of Vibrational Properties and Thermal Conductivity of Perovskites to Pressure

Songrui Hou [a], Richard B. Wilson [a,b,*], Chen Li [a,b,*].

[a] Materials Science and Engineering, University of California, Riverside, California 92521, USA

[b] Department of Mechanical Engineering, University of California, Riverside, California 92521, USA

*Correspondence should be sent to rwilson@ucr.edu and chenli@ucr.edu

Abstract

We study the response of $SrTiO_3$ and $KTaO_3$'s vibrational properties and thermal conductivity[1] Λ to pressurization. The goal is to improve understanding of the relationship between crystal structure, vibrational dynamics, and thermal conductivity in perovskites. We measure the thermal conductivity of $SrTiO_3$ and $KTaO_3$ up to 28 GPa by time-domain thermoreflectance. We also perform Raman scattering and stimulated Brillouin scattering measurements of $SrTiO_3$ and $KTaO_3$ to characterize changes in vibrational dynamics with pressure. The thermal conductivity of $SrTiO_3$ increases under pressure with a slope comparable to other perovskites whose thermal conductivity has been measured vs. pressure. Alternatively, the thermal conductivity of $KTaO_3$ has a stronger pressure dependence than that of other materials with similar crystal structure. We correlate pressure-induced changes in Raman and Brillouin spectra with pressure-induced changes in thermal conductivity. We show that pressure-induced changes in phonon lifetimes dominate the pressure dependence of thermal conductivity. This study provides benchmark knowledge on why Λ depends on pressure and improves understanding of structure/thermal-property relationships.

Keywords: $SrTiO_3$, $KTaO_3$, thermal conductivity, phonon anharmonicity, diamond anvil cell

[1] Abbreviation: thermal conductivity (Λ)

Introduction

Perovskite oxides are an important class of functional materials because small modifications in the crystal structure can cause dramatic changes in properties [1,2]. $SrTiO_3$ is a 'model' system for this kind of structure/property relationship due to its quantum paraelectric ground state, as well as its cubic-tetragonal phase transition at 105 K. As a result, the relationship between temperature, vibrational dynamics, and thermal transport in perovskites such as $SrTiO_3$ has been explored for more than half a century [3–7]. However, the question of how pressure-induced changes in vibrational dynamics affect Λ has received much less attention [8]. In many ways, pressure is a more effective experimental knob for changing vibrational dynamics than temperature. Phonons are quanta of lattice vibration and the main heat carriers in nonmetallic crystals [9]. Thermal conductivity from phonons is

$$\Lambda = \int_0^{\omega_m} \frac{1}{3} c(\omega) \cdot v(\omega)^2 \cdot \tau(\omega)\, d\omega, \qquad (1)$$

where $c(\omega)$ is the heat capacity per phonon of frequency ω, $v(\omega)$ is the phonon group velocity, and $\tau(\omega)$ is the phonon lifetime. All three parameters depend on vibrational dynamics. Temperature is only effective in tuning the frequency of some low-energy transverse optic phonons in perovskites [10,11]. Pressure will affect the frequency of nearly all phonon modes. By measuring both vibrational dynamics and thermal conductivity under pressure, we can determine how pressure-induced changes in vibrational dynamics affect thermal transport.

In this work, we measured the $\Lambda(P)$ of $SrTiO_3$ and $KTaO_3$ up to 28 GPa by time-domain thermoreflectance (TDTR) with a diamond anvil cell (DAC). We also performed Raman and stimulated Brillouin scattering measurements of vibrational properties vs. pressure.

$SrTiO_3$ and $KTaO_3$ were chosen for our study due to their similarities and differences. Both materials have similar crystal and vibrational structures. $SrTiO_3$ and $KTaO_3$ have a cubic structure under ambient conditions (space group: $Pm\bar{3}m$). Both crystals have soft TO phonon modes near Γ point in the Brillouin zone [11,12]. By soft modes, we mean that the frequencies of these modes decrease upon cooling. $SrTiO_3$ and $KTaO_3$ have different phase diagrams, which allows us to examine the effect of phase transition on vibrational and thermal properties. $SrTiO_3$ experiences a cubic-tetragonal phase transition upon cooling (~105 K at atmospheric pressure) or pressurization (~9.6 GPa at room temperature) [13]. $KTaO_3$ does not undergo a similar phase transition. As a result, $\Lambda(T)$ of $KTaO_3$ has a nearly $1/T$ dependence above 100 K,

while $SrTiO_3$ does not [3]. Other reasons we chose to study $SrTiO_3$ include that it is considered a model system for soft-phonon related phase transition phenomena [14] and that its phase transition upon compression is well documented and understood [13,15,16].

We observe that $\Lambda(P)$ of both $SrTiO_3$ and $KTaO_3$ increase linearly upon compression. Between 0 and 20 GPa, Λ of $SrTiO_3$ doubles. Across the same pressure range, Λ of $KTaO_3$ triples. Raman and Brillouin scattering suggest that $SrTiO_3$ experiences a phase transition at ~9.1 GPa. $KTaO_3$ does not change phase in the studied range of 0 to 30 GPa. The Raman modes of $SrTiO_3$ and $KTaO_3$ show similar stiffening under pressure. We compare the pressure-dependent thermal conductivity of $SrTiO_3$ and $KTaO_3$ with materials of similar crystal structure. The comparison shows that $SrTiO_3$ has a typical pressure dependence, while $KTaO_3$ has a stronger-than-typical pressure dependence. Significant changes in thermal conductivity imply significant changes in one, or all, of the following vibrational properties: (i) number of phonons, (ii) phonon group velocity, and (iii) phonon lifetime. Raman and Brillouin scattering measurements rule out (i) and (ii) as likely causes for the pressure-dependent thermal conductivity. Alternatively, measurements of the Brillouin frequency in $KTaO_3$ and $SrTiO_3$ suggest significant changes in phonon anharmonicity upon compression. Furthermore, the change is more than a factor of 2 larger in $KTaO_3$ than in $SrTiO_3$. Therefore, we conclude $d\Lambda/dP$ of $SrTiO_3$ and $KTaO_3$ are consequences of pressure-induced changes in phonon anharmonicity.

1. Materials and Methods

Sample Preparation

The $SrTiO_3$ and $KTaO_3$ are from the MTI Corporation. To prepare samples for diamond anvil cell measurements, we polished the samples down to thicknesses of 7 ± 2 μm. We used an optical microscope to estimate the final thickness after polishing. Then we used a needle to break the crystals into small pieces. We selected pieces with lateral dimensions of ~50-80 μm. We deposited an ~80-nm-thick Al or Ta film on the selected pieces. The metal film serves as an optical transducer for TDTR and stimulated Brillouin scattering experiments. Al is a good transducer for TDTR experiments conducted under ambient conditions. However, Al's thermoreflectance at 783 nm is a strong function of pressure and is small above 20 GPa [17]. Our motivation to carry out additional experiments with an α-Ta transducer is to verify that the observed trends are not related to the small thermoreflectance of Al in certain pressure ranges. The thermoreflectance of α-Ta is large at high pressures [17]. We deposited Ta at 800 °C to obtain α-phase Ta [18], which has

higher thermoreflectance than the β-phase Ta that results from room temperature deposition [17]. For Raman scattering measurements, we prepared samples that were not coated with a metal film.

We loaded the samples into DACs with a culet size of 300 μm. All measurements were made on the (100) surface of the samples. We loaded ruby spheres alongside the samples. The fluorescence spectrum of the Ruby was used as a pressure gauge. We used silicone oil (polydimethylsiloxane) as the pressure medium for most measurements. We used Ne as the pressure medium in one set of Brillouin scattering measurements on $SrTiO_3$ (yellow circles in Figure 3(b)).

We used 250-μm thick stainless-steel gaskets and pre-indented them in our DAC to a thickness between 30 and 60 μm. Then we drilled holes with a diameter of ~170 μm at the center of the indentations using an electro-discharge machine. The holes serve as containers for the samples, ruby spheres, and pressure medium. The schematics of the DAC assembly and sample geometry are shown in Figure 1. Further details can also be found in our previous work [19]. Plastic deformation/sample distortion can happen if the sample is not prepared carefully. We discuss the potential effects of plastic deformation/sample distortion under pressure and how to avoid it in the Supplementary Material.

Raman Scattering

We measured the Raman spectrum of $SrTiO_3$ and $KTaO_3$ from 100 to 1200 cm^{-1}. We first measure the ambient Raman spectrum in the air. At high pressure, we collect the spectrum inside a DAC with silicone oil as the pressure medium. To exclude the Raman signals of the pressure medium, we also measured the Raman spectrum of the pressure medium along with our samples as the pressure changes. The exciting laser has a 532-nm wavelength. We used a monochromator (Acton SpetraPro-2500i) to collect the scattered light. We placed a long-pass edge filter (Semrock LP03-532RE-25) in front of the spectrometer to filter out background noise.

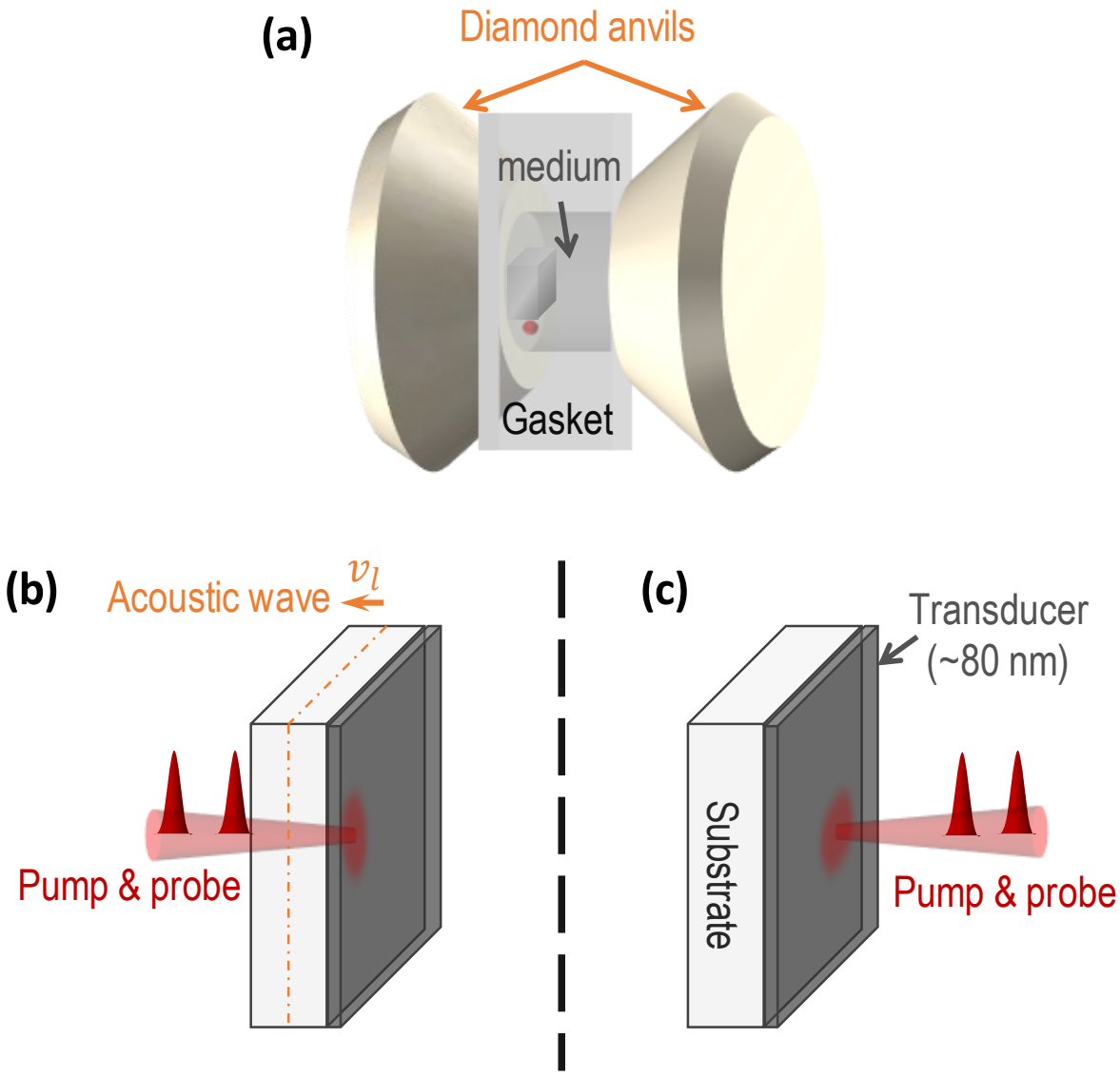

Figure 1. Schematics of the diamond anvil cell (DAC) assembly and experimental geometries. (a) The samples along with the ruby spheres are loaded into the DAC chamber. (b) For stimulated Brillouin scattering measurements, the pump and probe beams impinge on the substrate side of the sample. (c) For TDTR measurements, the pump and probe beams impinge on the transducer side of the sample.

TDTR and Stimulated Brillouin Scattering Measurements

The schematics of stimulated Brillouin scattering and TDTR measurements are shown in Figures 1(b) and 1(c). We performed TDTR measurements of the thermal conductivities of $SrTiO_3$ and $KTaO_3$ at pressures between 0 and 28 GPa. TDTR is a well-established pump probe technique for thermal property characterization [20]. Details of our TDTR setup can be found in Ref. [21]. Pressure is calibrated using the pressure-dependent shift of the R1 line in the ruby fluorescence spectrum [22].

We also performed stimulated Brillouin scattering measurements using our TDTR setup. For Brillouin measurements of the perovskite crystals, the laser beams impinged through the substrate side of the sample. The beams went through pressure media, samples ($SrTiO_3$ or $KTaO_3$), and then hit the transducer surface. At all pressures that we studied, $SrTiO_3$ and $KTaO_3$ are insulators with band gaps larger than 3 eV [23,24], so they are transparent to laser beams. For Brillouin measurements of the silicone oil, the laser beams impinged on the transducer side of the sample. The beams went through the silicone oil and then were reflected from the transducer. In both sets of measurements, the laser beams were perpendicular to the sample. When the pump beam heats the transducer surface (Al or Ta in our experiments), it launches a strain wave into the perovskite substrates or silicone oil. The strain wave front moves at the longitudinal speed of sound of the samples. Both the strain wave and the transducer can reflect the subsequent probe beam. These two reflected probe beams interfere with each other and cause Brillouin oscillations in the in-phase voltage signal V_{in} [25]. We use the measured Brillouin frequencies of $SrTiO_3$ and $KTaO_3$ as a measure of the longitudinal speed of sound in these materials. We use the Brillouin frequency of silicone oil as an additional measure of pressure [26] to complement our ruby fluorescence measurements.

We use a bidirectional heat diffusion model to analyze the collected TDTR data [27]. The bidirectional model accounts for heat flow from the transducer to both the substrate and silicone oil. The thermal conductivity, heat capacity, and thickness of each layer are the input parameters in the heat diffusion model. Therefore, we must estimate how these parameters evolve with pressure to interpret our TDTR data. We describe how we account for the pressure dependence of all parameters in the Supplementary Material.

Results

$SrTiO_3$ has a cubic phase (space group: $Pm\bar{3}m$) below 9.1 GPa. The cubic symmetry of $SrTiO_3$ forbids first-order Raman scattering. However, $SrTiO_3$ has two broad bands (210 to 440 cm^{-1}, 550 to 780 cm^{-1}) that are attributable to second-order Raman scattering [13,28]. The two broad bands blue shift upon

compression. At room temperature and above 9.1 GPa, $SrTiO_3$ transforms into a tetragonal phase (space group: *I*4/*mcm*). In this phase, several phonon modes are Raman active [13]. At pressures above 9.1 GPa, we observe two peaks form near 162 and 466 cm^{-1}, see Figure 2(a). These two peaks are first-order Raman peaks with $E_g + B_{1g}$ symmetry and indicate the cubic-tetragonal phase transition.

$KTaO_3$ has cubic symmetry (space group: $Pm\bar{3}m$), so all the features in the Raman spectra are second order [29]. As the pressure increases, all the peaks shift to higher wavenumbers, and, unlike $SrTiO_3$, we do not observe any new Raman peak form at higher pressures (Figure 2(b)). This is consistent with our expectation that $KTaO_3$ does not undergo a phase transition in the studied pressure range.

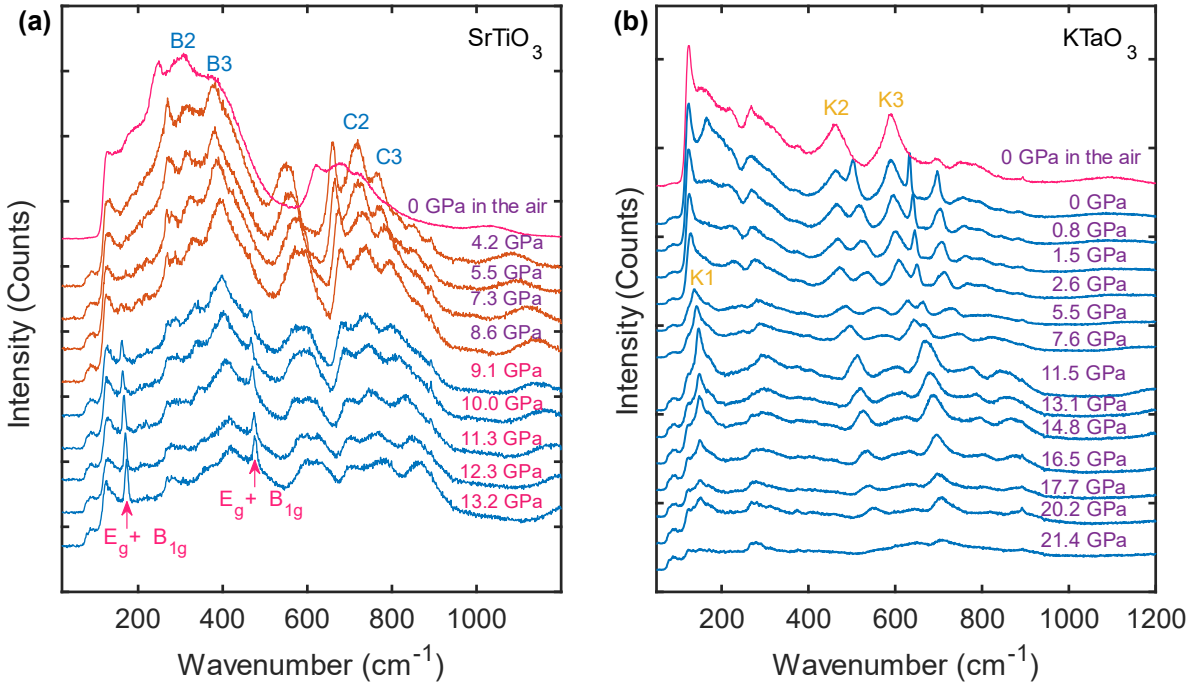

Figure 2. Raman spectra of $SrTiO_3$ and $KTaO_3$ under pressure. In panel (a), the peak near 600 cm^{-1} is a Raman peak from silicone oil. The $SrTiO_3$ Raman peak near 700 cm^{-1} overlaps with a silicone oil peak. In panel (b), peaks around 170 cm^{-1}, 500 cm^{-1}, 630 cm^{-1}, and 700 cm^{-1} are Raman peaks from silicone oil. The $KTaO_3$ Raman peak near 260 cm^{-1} overlaps with a silicone oil peak. Detailed comparison between the $KTaO_3$ spectrum with and without silicone oil can be found in Supplementary Figure S5.

Raman shifts vs. pressure for selected Raman peaks are shown in Figure 3(a). The Raman shifts reflect increases in the frequency of the phonons responsible for Raman scattering. Therefore, these measurements

provide a measure of the stiffening of vibrational dynamics with pressure. We excluded Raman peaks of the pressure medium (silicone oil, polydimethylsiloxane. Its pressure-dependent Raman spectra are shown in Supplementary Figure S5(a)). We followed Ref. [13] and label the selected $SrTiO_3$ peaks B2, B3, C2, C3 (these labels are arbitrary). For $KTaO_3$, we labeled the selected peaks as K1, K2, K3. We only tracked the B2 peak of $SrTiO_3$ up to 9.1 GPa due to degradation of its signal quality. The K1 peak of $KTaO_3$ drops below the transition width of our edge filter below 5.5 GPa. The frequencies of the selected peaks mostly increase linearly upon compression. The pressure dependence of each Raman mode is shown in Figure 3(a). We observe that shifts of Raman peaks of $SrTiO_3$ and $KTaO_3$ have a similar pressure dependence. At 13 GPa, all selected peaks increase by ~15%. Our pressure-dependent Raman results for $SrTiO_3$ are mostly consistent with the results reported in Ref. [13], as shown by the comparison in Supplementary Figure S6. The main difference is that our C3 Raman mode shows a larger pressure dependence than the results in Ref. [13].

The Brillouin frequency of $SrTiO_3$ shows a decrease within 2 GPa around the phase transition (~9 GPa in Figure 3(b)). This anomaly is consistent with previous reports for the elastic constants of $SrTiO_3$ vs. pressure [16]. The observed transition pressure is also consistent with our Raman results in Figure 2(a) and 3(a). For $KTaO_3$, we observe a monotonically increasing Brillouin frequency. The Brillouin frequency is

$$f = 2Nv_l / \lambda, \qquad (2)$$

Where N is the index of refraction of the sample, v_l is the longitudinal speed of sound of the sample, and λ is the excitation wavelength (783 nm in our experiments).

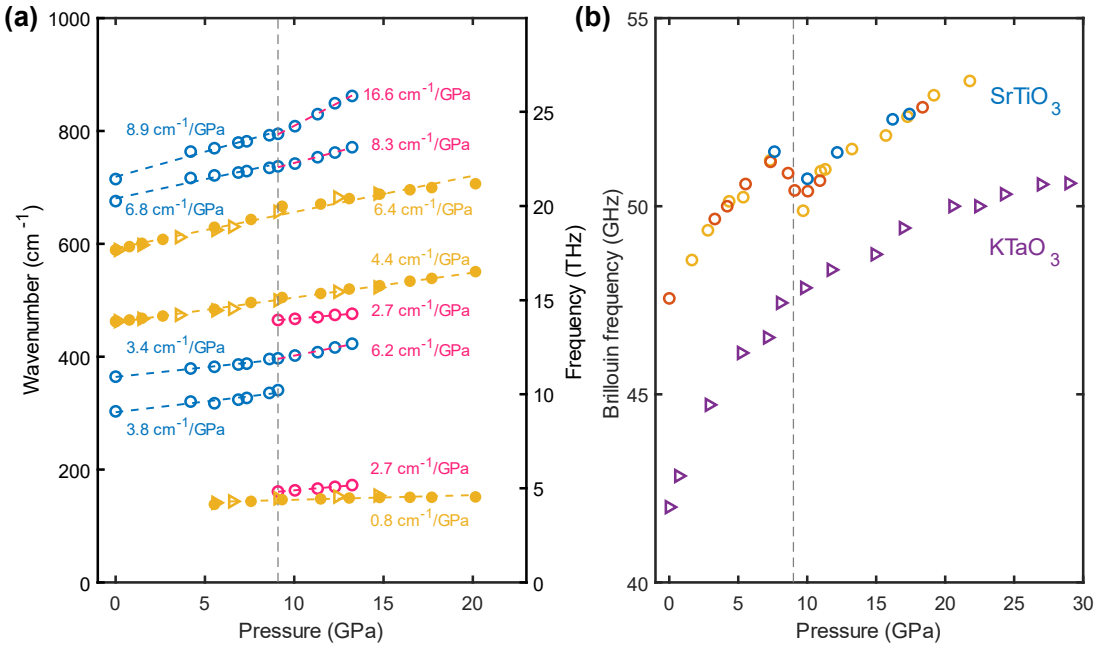

Figure 3. Scattering data vs. pressure for $SrTiO_3$ and $KTaO_3$. (a) Frequencies of selected Raman peaks vs. pressure. Circles and triangles are data collected during pressure increase and pressure decrease, respectively. Dashed lines are linear fittings to the data. Each fitting is labelled with its slope. For $SrTiO_3$ the slope is determined separately for cubic vs. tetragonal phases. (b) Brillouin frequency vs. pressure in the [100] direction. The circles are data collected on $SrTiO_3$. Different colors represent different pieces of $SrTiO_3$. The triangles are $KTaO_3$. The vertical dashed line in (a) and (b) show the phase transition pressure of $SrTiO_3$.

We observe linearly increasing thermal conductivity as the pressure increases in both $SrTiO_3$ and $KTaO_3$ (Figure 4). We obtain similar thermal conductivity results with different transducers and laser spot sizes. The gradient, $d\Lambda/dP$, is ~0.61 W m^{-1} K^{-1} GPa^{-1} for $SrTiO_3$ in the cubic phase and ~0.37 W m^{-1} K^{-1} GPa^{-1} for $SrTiO_3$ in the tetragonal phase. The thermal conductivity of a $SrTiO_3$ sample (red dots in Figure 4) is ~20% lower than the other three. A possible explanation is that the polishing procedure necessary to prepare samples for DAC measurements caused minor plastic deformation in that sample near its surface. Two sets of our $SrTiO_3$ data (blue and gray dots in Figure 4(a)) show a ~10% decrease between 8 and 13 GPa. When the transducer is switched to Ta (magenta markers), the decrease is reduced to ~5%. In the red-dot dataset, there is no decrease at all. The small change in thermal conductivity we observed in some data sets near the phase transition may be related to the group velocity drop at the phase transition (Figure 3(b)). We note that the 5-10% changes we observe are comparable to the overall jitter in our thermal

conductivity results. Therefore, if there is a change to thermal conductivity induced by the phase transition, the change's magnitude is smaller than that we can reliably resolve via TDTR in a DAC. Recent work on $SrTiO_3$ reports that their sample has a sharp drop of -25% at phase transition (~6 GPa) [30]. Their data also show a change in the slope at phase transition (~0.54 and ~0.34 W m^{-1} K^{-1} GPa^{-1} for cubic and tetragonal $SrTiO_3$, respectively). Their slope values are ~10% lower than our results. $d\Lambda/dP$ = 1.2 W m^{-1} K^{-1} GPa^{-1} for $KTaO_3$. The relative change at 20 GPa, $\Lambda(20\ GPa)/\Lambda(1\ bar)$, is ~200% for $SrTiO_3$, and ~300% for $KTaO_3$. The data of pressure-dependent interface conductance between transducers and substrates are shown in Figure S7. Examples of TDTR data are shown in Figure S8 and S9.

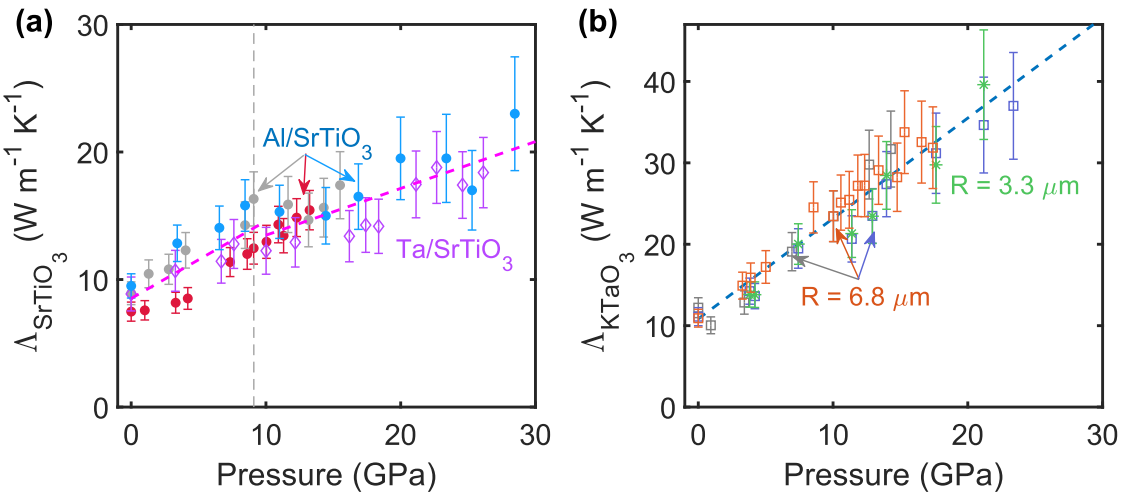

Figure 4. Thermal conductivity of $SrTiO_3$ and $KTaO_3$ under pressure measured by TDTR. (a) We measure the $\Lambda(P)$ of $SrTiO_3$ with two different optical transducers: Al and Ta. Three datasets are measured with Al (blue, red, and gray), and one is Ta (purple). (b) We measure the $\Lambda(P)$ of $KTaO_3$ with two different spot sizes (6.8 and 3.3 μm). Three datasets are measured using 6.8 μm laser spot size (orange, blue, gray), and one is 3.3 μm (green). Error bars here denote our estimate of ~13-20% uncertainty that arises from uncertainty in input parameters for the heat diffusion model we use to analyze time-domain thermoreflectance data. Detailed uncertainty analysis can be found in the Supplementary Material. The dashed lines are linear fittings to the data. The vertical dash line shows the phase-transition pressure of $SrTiO_3$.

Discussion

Our results in Figures 2-4 show that both the vibrational dynamics and thermal conductivity have strong pressure dependences. And, notably, Λ of $SrTiO_3$ does not have an abrupt change at phase transition. We now focus on understanding these observations.

Why does the phase transition at 9.1 GPa not cause a more significant change in $SrTiO_3$'s thermal conductivity? Phase transitions sometimes cause abrupt changes in thermal conductivity. For example, $\Lambda(P)$ of NaCl drop by 60% at the phase-transition pressure of 30 GPa [31]. However, different from the first-order phase transition in NaCl, the cubic-tetragonal phase transition in $SrTiO_3$ is a second-order displacive phase transition [32]. $SrTiO_3$'s transition is related to the rotation of TiO_6 octahedral, which is continuous and gradual. The tetragonal distortion is small below 30 GPa (c/a = 1.01 at 30 GPa) [13]. No abrupt change in $\Lambda(T)$ of $SrTiO_3$ at ambient pressure is observed at the phase-transition temperature of 105 K [3,4]. Therefore, the fact that we did not observe clear evidence of a significant drop in $\Lambda(P)$ of $SrTiO_3$ at 9.1 GPa is not surprising.

Now we evaluate the magnitude of $d\Lambda/dP$ we observe for $SrTiO_3$ and $KTaO_3$. To do this, in Figure 5(c) we compare the increase in relative thermal conductivity of different materials at 20 GPa, $\Lambda(20\ GPa)/\Lambda(1\ bar)$. Most of the materials that we include for comparison are oxides and have a cubic crystal structure. All materials in Figure 5(c) display a monotonically increasing thermal conductivity under compression. $SrTiO_3$ has a pressure dependence of Λ similar to most materials, while $KTaO_3$ has a stronger pressure dependence than other materials.

Pressure-induced changes to thermal conductivity are caused by changes in heat capacity per mode, phonon group velocity, and phonon lifetime, see Eq. (1). To explore why $SrTiO_3$ and $KTaO_3$ have different pressure dependence in $\Lambda(P)$, we evaluate changes of these three parameters. To do this, we consider predictions of the Leibfried-Schlömann equation (LS) for the heat capacity, phonon group velocity, and phonon lifetime change with pressure. Then, we consider what our Raman and Brillouin scattering measurements vs. pressure imply for the pressure dependence of phonon heat capacity, phonon group velocity, and phonon lifetime. Finally, we consider the predictions of previous theoretical studies that utilized first-principles methods to calculate vibrational dynamics [5,6].

The LS equation is commonly used to explain observed trends for $\Lambda(P)$ in nonmetallic crystals such as NaCl [31] and MgO [33]. The LS equation approximates c, ν, and τ in Eq. (1) using properties that can be

extracted from volume-pressure equation of states (*V-P* EOS) [34]. The volumetric heat capacity is assumed to be $C \propto 1/V$. Group velocity v is parameterized as $v = \sqrt{K_T/\rho} \propto \delta\theta$. Phonon mean free path is set to be $l \propto \delta \ / \ T\alpha\gamma$ [9]. Here, K_T is the isothermal bulk modulus defined as $K_T = -dP \ / \ d\ ln\, V$, and α is the volumetric thermal expansion coefficient which can be calculated by $\alpha = C\gamma \ / \ K_T$. Plugging these approximations into Eq. (1) yields

$$\Lambda = \frac{B\bar{M}\delta\theta^3}{T\gamma 2}. \qquad (3)$$

Here B is a constant, $\bar{M}$ is the average mass of an atom in the crystal, δ^3 is the average volume occupied by one atom in the crystal, θ is the Debye temperature, T is temperature, and γ is the Grüneisen parameter. δ, θ, and γ are all pressure dependent. To calculate Λ vs. P using Eq. (3), we follow the procedures in Ref. [34] to extract these parameters from the *V-P* EOS. The evolution of δ, θ, γ with pressure depends on the first, second, and third derivatives of the *V-P* EOS. We adopt the third-order Birch-Murnaghan equation of states (B-M EOS) in Ref. [13] to calculate the pressure dependent δ, θ, and γ. Cubic and tetragonal B-M EOS produce different fittings for $SrTiO_3$ (see Figure 5(a)). Due to the lack of experimental EOS for $KTaO_3$, we assume that $KTaO_3$ follows the cubic B-M EOS of $SrTiO_3$. This assumption is reasonable because of their similar crystal structure. The results of the first-principles calculations [35] support this assumption (see Figure 5(b)).

The LS equation agrees reasonably well with our experimental $\Lambda(P)$ of $KTaO_3$ and $SrTiO_3$. Note that we choose different values for the constant B in Eq. (3) for our predictions in Figure 5(a) for cubic and tetragonal $SrTiO_3$. For cubic $SrTiO_3$, we set B to make Eq. (3) agree with Λ at ambient conditions. For tetragonal $SrTiO_3$, we set B to agree with Λ at 10 GPa, the lowest pressure that we observe $SrTiO_3$ to be in the tetragonal phase. Therefore, the difference in the LS equation curves for cubic vs. tetragonal $SrTiO_3$ at 10 GPa is not a prediction of the LS equation. Instead, the abrupt drop in the LS equation curves at 10 GPa reflects the fact that the LS equation predicts a higher $d\Lambda/dP$ (0.73 W m^{-1} K^{-1} GPa^{-1}) for cubic $SrTiO_3$ than what we experimentally observe.

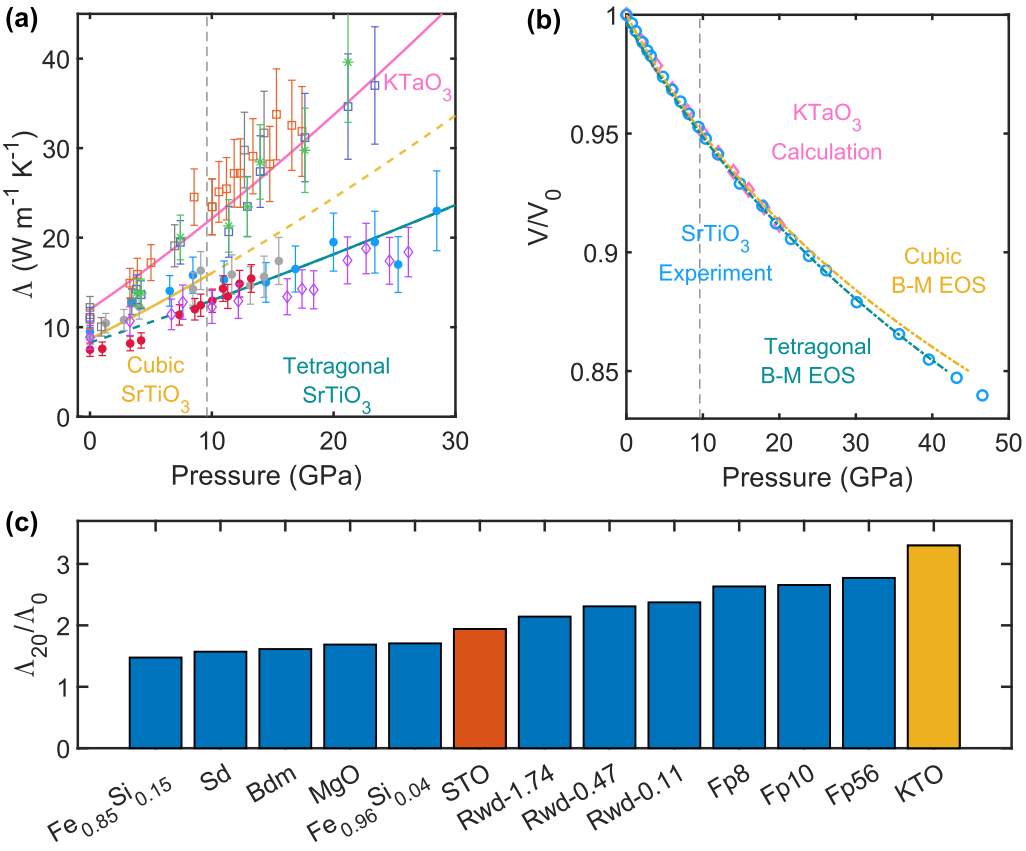

Figure 5. (a) Predictions of the LS equation (solid lines) in comparison to measured thermal conductivity of $SrTiO_3$ and $KTaO_3$ (markers). The solid pink line is the prediction of the LS equation for $KTaO_3$. The yellow and green lines are the LS predictions using cubic and tetragonal B-M EOS for $SrTiO_3$, respectively. (b) Equations of states of $SrTiO_3$ and $KTaO_3$. V / V_0 is the unit cell volume relative to the ambient volume V_0. Blue circles are experimental data of $SrTiO_3$ from Ref. [13]. Yellow and green dash-dotted lines are B-M EOS fittings to the experimental data, also from Ref. [13]. Pink diamonds are calculated EOS of $KTaO_3$ from Ref. [35]. The vertical dashed line represents the cubic-tetragonal phase transition in $SrTiO_3$. (c) The ratio between thermal conductivity at 20 GPa and atmospheric pressure for various materials. Materials for comparison include Fe-Si alloys [36], MgO [33], ferropericlase (Fp) [37], bridgmanite (Bdm) [38], ringwoodite (Rwd) [39], siderite (Sd) [40], $SrTiO_3$ (STO) and $KTaO_3$ (KTO).

The LS equation predicts that most of the change in the thermal conductivity of $SrTiO_3$ and $KTaO_3$ upon compression to 20 GPa is due to changes in the lifetimes of phonons. According to their *V-P* EOS, upon compression to 20 GPa, V decreases by 9% for $SrTiO_3$ and $KTaO_3$ at 20 GPa (Figure 5(b)). One of the

standard methods to calculate the Debye temperature is from elastic constants [41], $\theta \propto \sqrt{\delta K_T}$, which can be calculated from the first derivative of *V-P* EOS. Analyzing the *V-P* EOS of $SrTiO_3$ and $KTaO_3$ in Ref. [13], we find θ increases by 20% for $SrTiO_3$ and 30% for $KTaO_3$. The LS equation uses the "Slater γ", which is defined as $\gamma = \frac{1}{2}\frac{dK_T}{dP} - \frac{1}{6}$ [42]. By calculating the second derivative of *V-P* EOS, we find that Slater γ decreases by 10% for $SrTiO_3$ and 13% for $KTaO_3$. Therefore, for $SrTiO_3$, the LS equation credits 10%, 15%, and 60% of the increase in Λ to changes in heat capacity, group velocity, and phonon mean free path, respectively. For $KTaO_3$, the numbers are 10%, 25%, 100% accordingly. We note that while the first and second derivatives of the EOS are straightforward to extract from experimental data, the third derivatives are not. Therefore, some skepticism is warranted for the LS equation prediction for $d\Lambda/dP$.

We now turn our attention to what our scattering measurements in Figures 2 and 3 imply for the heat capacity per phonon mode in Eq. (1). The heat capacity per mode is

$$c(q) = D(q)\hbar\omega_q \frac{\partial n(\omega_q)}{\partial T}. \qquad (4)$$

Here, q is phonon wavevector, $D(q)$ is the density of states with wavevector q, and *n* is the Bose-Einstein distribution. The primary way that pressure affects $c(q)$ is through mode stiffening. Upon compression to 20 GPa, the Raman frequencies of $SrTiO_3$ and $KTaO_3$ increase by up to ~20%, see Figure 3(a). First-principles calculations for $SrTiO_3$ predict that, at room temperature, heat is carried primarily by phonons with ω_q between 0 and 15 THz [43]. For modes with ω_q = 5, 10, and 15 THz at 0 GPa, a ~20% increase in ω_q upon compression to 20 GPa will lead to a decrease in $\hbar\omega_q\frac{\partial n}{\partial T}$ by 2, 7, and 11%, respectively. So, our experimental data on the vibrational dynamics suggest changes in $c(q)$ will be small, in agreement with the LS-equation prediction described above. First-principles calculations predict that total heat capacities of $SrTiO_3$ and $KTaO_3$ are nearly constant up to 20 GPa [35,44] (see Figure S1(d)).

Now we consider the effect of pressure on group velocity. Our Brillouin frequency data allow us to calculate the group velocity of low-energy longitudinal acoustic (LA) phonons along [100] direction. To calculate v_l, we need to estimate the index of refraction *N* under pressure. To our knowledge there is no experimental data of *N* of $SrTiO_3$ and $KTaO_3$ under pressure. First-principles calculations suggest that *N* has nearly negligible pressure dependence. The *N* of $KTaO_3$ decreases by 4% at 40 GPa [45]. The *N* of $SrTiO_3$ decreases by 3% at 60 GPa [23]. Therefore, since the effect of pressure is small, for simplicity we assume d*N*/*dP* ≈ 0. Then the longitudinal group velocity increases by ~10% for $SrTiO_3$ and ~20% for

$KTaO_3$ at 20 GPa (Figure 3(b) and Eq. (2)). This compares favorably with the LS-equation estimates described above of a 15% and 25% increase in group velocity for $SrTiO_3$ and $KTaO_3$, respectively. So, we conclude that, while velocity changes are larger than heat capacity changes, their effects are still minor. Pressure-induced changes to phonon velocity cannot explain the factor of 2 and 3 increase we see in Λ of $SrTiO_3$ and $KTaO_3$ upon compression to 20 GPa.

We now turn our attention to what information our Brillouin measurements have regarding phonon lifetimes. One way to estimate phonon lifetime changes is to consider the mode Grüneisen parameter γ of the phonons. γ is defined as the relative change in the frequency (ν) of a phonon due to a relative change in volume (V),

$$\gamma = -\frac{d\,ln\,\nu}{d\,ln\,V}. \qquad (5)$$

We fit $\nu(P)$ by a line using the nearest three data points at a given pressure, use the Birch-Murnaghan EOS to convert $\nu(P)$ to $\nu(V)$, and calculate γ by Eq. (5). The γ for $SrTiO_3$ drops by 50% at 20 GPa (2.25 at 0 GPa and 1.09 at 20 GPa). And the γ for $KTaO_3$ drops by 80% at 20 GPa (3.62 to 0.65). The Grüneisen parameter is a measure of phonon anharmonicity, and, in general, phonon lifetimes decrease with increasing anharmonicity. So, our Brillouin data provide evidence that pressure induced changes in phonon lifetime are significant in both $SrTiO_3$ and $KTaO_3$, and, that the changes are larger in $KTaO_3$. Based on predictions and our experimental data, we conclude that pressure-induced changes in Λ are mainly driven by changes in phonon lifetime. This explains the larger pressure dependence we observe for Λ of $KTaO_3$ than $SrTiO_3$, see Figure 4.

Why do the phonon lifetimes and phonon anharmonicity change more with pressure in $KTaO_3$ than in $SrTiO_3$? It is known that $KTaO_3$ is close to a ferroelectric phase transition at ambient conditions, while $SrTiO_3$ is relatively stable [5,6,46]. First-principles calculations show that displacements of Ta and O atoms in $KTaO_3$ occur in nonparabolic potential wells, indicating large anharmonicity [46]. The calculations suggest that volume contraction will make potential wells parabolic and the crystal lattice stable. Also, first-principles calculations suggest that phonon frequencies of low-lying TO modes near Γ point in $KTaO_3$ are more sensitive to pressure than those of $SrTiO_3$. For low-lying TO modes in $KTaO_3$, a 1% volume expansion can decrease their frequencies by 60% [5]. The corresponding Grüneisen parameter is ~50. For $SrTiO_3$, a 6% volume expansion decreases the frequencies of low-lying TO modes by only 30% [6]. The corresponding γ is only ~5. For $KTaO_3$ under ambient conditions, the low-lying optic

phonon branch has a frequency similar to that of the longitudinal acoustic phonon branch near Γ point [5]. This feature can produce a large phase space for phonon-phonon scattering since selection rules (conservation of energy and momentum) can be easily satisfied [47]. Pressurization drives low-lying TO branch away from LA branch in frequency. The increase of the frequency gap makes satisfying selection rules harder and can therefore be expected to decrease the phonon-phonon scattering phase space of $KTaO_3$.

Conclusions

We measured the $\Lambda(P)$ of $SrTiO_3$ and $KTaO_3$ up to 28 GPa by time-domain thermoreflectance with diamond anvil cells. We observe the $\Lambda(P)$ of $KTaO_3$ has an unusually large pressure dependence, while $SrTiO_3$ has a typical pressure dependence. By correlating thermal conductivity and scattering measurements, we show that the different pressure dependence in $\Lambda(P)$ is caused by differences in how the phonon lifetimes evolve with pressure. Furthermore, we show that most of the observed change in Λ is caused by changes in phonon lifetime. We find that the predictions of the LS equation for the thermal conductivity and vibrational properties agree fairly well with our observations. Our observation that modest changes in phonon frequencies of ~10-20% cause significant changes in Λ and average phonon lifetimes of 200-300% has important implications for a variety of fields. Understanding the relationship between vibrational spectra and thermal conductivity is an active area of research in the heat transfer community [19,47], with the ultimate goal of identifying materials with high thermal conductivities for thermal management applications [48]. Our findings also have relevance to the science of thermoelectric materials. Many perovskites are promising thermoelectric materials [49,50], and understanding the relationship between vibrational properties, phonon lifetimes, and thermal conductivity is important for engineering materials with low thermal conductivity [51]. Finally, our finding that changes in phonon lifetime dominate $d\Lambda/dP$ is relevant to ongoing efforts in the geophysics community to understand the thermal balance and history of the Earth [52]. Many minerals in Earth's mantle have a perovskite crystal structure, e.g., bridgmanite, and knowledge of how pressure and temperature affect thermal conductivity is crucial for modelling heat flux at the core-mantle boundary [52].

Acknowledgement

This research was supported as part of ULTRA, an Energy Frontier Research Center funded by the U.S. Department of Energy (DOE), Office of Science, Basic Energy Sciences (BES), under Award #DE-

SC0021230 (TDTR measurements), and by the National Science Foundation (NSF) under Awards #1847632 ((Brillouin measurements and thermal modelling) and #1750786 (Raman scattering measurements). Use of the COMPRES-GSECARS gas loading system was supported by COMPRES under NSF Cooperative Agreement EAR -1606856 and by GSECARS through NSF grant EAR-1634415 and DOE grant DE-FG02-94ER14466. This research used resources of the Advanced Photon Source, a U.S. Department of Energy (DOE) Office of Science User Facility operated for the DOE Office of Science by Argonne National Laboratory under Contract No. DE-AC02-06CH11357.

References

[1] J.H. Haeni, P. Irvin, W. Chang, R. Uecker, P. Reiche, Y.L. Li, S. Choudhury, W. Tian, M.E. Hawley, B. Craigo, A.K. Tagantsev, X.Q. Pan, S.K. Streiffer, L.Q. Chen, S.W. Kirchoefer, J. Levy, D.G. Schlom, Room-temperature ferroelectricity in strained SrTiO3, 430 (2004) 4.

[2] L. Maerten, A. Bojahr, M. Gohlke, M. Rössle, M. Bargheer, Coupling of GHz Phonons to Ferroelastic Domain Walls in SrTiO 3, Phys. Rev. Lett. 114 (2015) 047401. https://doi.org/10.1103/PhysRevLett.114.047401.

[3] E.F. Steigmeier, Field Effect on the Cochran Modes in SrTiO_3 and KTaO_3, Physical Review. 168 (n.d.) 523–530. https://doi.org/10.1103/PhysRev.168.523.

[4] V. Martelli, J.L. Jiménez, M. Continentino, E. Baggio-Saitovitch, K. Behnia, Thermal Transport and Phonon Hydrodynamics in Strontium Titanate, Phys. Rev. Lett. 120 (2018) 125901. https://doi.org/10.1103/PhysRevLett.120.125901.

[5] Y. Fu, D.J. Singh, Thermal conductivity of perovskite KTaO 3 and PbTiO 3 from first principles, Phys. Rev. Materials. 2 (2018) 094408. https://doi.org/10.1103/PhysRevMaterials.2.094408.

[6] A.O. Fumega, Y. Fu, V. Pardo, D.J. Singh, Understanding the lattice thermal conductivity of SrTiO 3 from an *ab initio* perspective, Phys. Rev. Materials. 4 (2020) 033606. https://doi.org/10.1103/PhysRevMaterials.4.033606.

[7] R. Shayduk, J. Hallmann, A. Rodriguez-Fernandez, M. Scholz, W. Lu, U. Bösenberg, J. Möller, A. Zozulya, M. Jiang, U. Wegner, R.-C. Secareanu, G. Palmer, M. Emons, M. Lederer, S. Volkov, I. Lindfors-Vrejoiu, D. Schick, M. Herzog, M. Bargheer, A. Madsen, Femtosecond x-ray diffraction study of multi-THz coherent phonons in $SrTiO_3$, Appl. Phys. Lett. 120 (2022) 202203. https://doi.org/10.1063/5.0083256.

[8] W. Hsieh, F. Deschamps, T. Okuchi, J. Lin, Reduced lattice thermal conductivity of Fe-bearing bridgmanite in Earth's deep mantle, J. Geophys. Res. Solid Earth. 122 (2017) 4900–4917. https://doi.org/10.1002/2017JB014339.

[9] J.M. Ziman, Electrons And Phonons: The Theory of Transport Phenomena in Solids, 1st ed., Oxford University Press, London, 1963.

[10] R.A. Cowley, Lattice Dynamics and Phase Transitions of Strontium Titanate, Phys. Rev. 134 (1964) A981–A997. https://doi.org/10.1103/PhysRev.134.A981.

[11] G. Shirane, R. Nathans, V.J. Minkiewicz, Temperature Dependence of the Soft Ferroelectric Mode in KTa O 3, Phys. Rev. 157 (1967) 396–399. https://doi.org/10.1103/PhysRev.157.396.

[12] Y. Yamada, G. Shirane, Neutron Scattering and Nature of the Soft Optical Phonon in SrTiO3, J. Phys. Soc. Jpn. 26 (1969) 396–403. https://doi.org/10.1143/JPSJ.26.396.

[13] M. Guennou, P. Bouvier, J. Kreisel, D. Machon, Pressure-temperature phase diagram of SrTiO 3 up to 53 GPa, Phys. Rev. B. 81 (2010) 054115. https://doi.org/10.1103/PhysRevB.81.054115.

[14] M.A. Carpenter, Elastic anomalies accompanying phase transitions in (Ca,Sr)TiO3 perovskites: Part I. Landau theory and a calibration for SrTiO3, American Mineralogist. 92 (2007) 309–327. https://doi.org/10.2138/am.2007.2295.
[15] S.-C. Weng, R. Xu, A.H. Said, B.M. Leu, Y. Ding, H. Hong, X. Fang, M.Y. Chou, A. Bosak, P. Abbamonte, S.L. Cooper, E. Fradkin, S.-L. Chang, T.-C. Chiang, Pressure-induced antiferrodistortive phase transition in $SrTiO_3$: Common scaling of soft-mode with pressure and temperature, EPL. 107 (2014) 36006. https://doi.org/10.1209/0295-5075/107/36006.
[16] C. Zhang, F. Li, X. Wei, M. Guo, Y. Wei, L. Li, X. Li, Q. Zhou, Abnormal Elastic Changes for Cubic-Tetragonal Transition of Single-Crystal $SrTiO_3$, Chinese Phys. Lett. 39 (2022) 096201. https://doi.org/10.1088/0256-307X/39/9/096201.
[17] W.-P. Hsieh, D.G. Cahill, Ta and Au(Pd) alloy metal film transducers for time-domain thermoreflectance at high pressures, Journal of Applied Physics. 109 (2011) 113520. https://doi.org/10.1063/1.3592882.
[18] L.A. Clevenger, A. Mutscheller, J.M.E. Harper, C. Cabral, K. Barmak, The relationship between deposition conditions, the beta to alpha phase transformation, and stress relaxation in tantalum thin films, Journal of Applied Physics. 72 (1992) 4918–4924. https://doi.org/10.1063/1.352059.
[19] S. Hou, B. Sun, F. Tian, Q. Cai, Y. Xu, S. Wang, X. Chen, Z. Ren, C. Li, R.B. Wilson, Thermal Conductivity of BAs under Pressure, Adv Elect Materials. (2022) 2200017. https://doi.org/10.1002/aelm.202200017.
[20] D.G. Cahill, Analysis of heat flow in layered structures for time-domain thermoreflectance, Review of Scientific Instruments. 75 (2004) 5119–5122. https://doi.org/10.1063/1.1819431.
[21] M.J. Gomez, K. Liu, J.G. Lee, R.B. Wilson, High sensitivity pump–probe measurements of magnetic, thermal, and acoustic phenomena with a spectrally tunable oscillator, Review of Scientific Instruments. 91 (2020) 023905. https://doi.org/10.1063/1.5126121.
[22] H.K. Mao, J. Xu, P.M. Bell, Calibration of the ruby pressure gauge to 800 kbar under quasi-hydrostatic conditions, Journal of Geophysical Research. 91 (1986) 4673. https://doi.org/10.1029/jb091ib05p04673.
[23] A. Batool, M.A. Faridi, Q. Mahmood, B. Ul Haq, A. Laref, S.E. Awan, The pressure-induced indirect to direct bandgap transition and thermoelectric response in SrTiO3: An ab-initio study, Journal of Physics and Chemistry of Solids. 123 (2018) 70–75. https://doi.org/10.1016/j.jpcs.2018.07.008.
[24] X. Liu, W. Lv, C. Chen, W. Yang, J. Han, J. Lin, H. Sun, Structural, electronic and optical properties of KTaO3 under high pressure based on first-principles, Materials Science in Semiconductor Processing. 138 (2022) 106248. https://doi.org/10.1016/j.mssp.2021.106248.
[25] C. Thomsen, H.J. Maris, J. Tauc, Picosecond acoustics as a non-destructive tool for the characterization of very thin films, Thin Solid Films. 154 (1987) 217–223.
[26] G.T. Hohensee, R.B. Wilson, D.G. Cahill, Thermal conductance of metal-diamond interfaces at high pressure, Nature Communications. 6 (2015) 1–9. https://doi.org/10.1038/ncomms7578.
[27] A. Schmidt, M. Chiesa, X. Chen, G. Chen, An optical pump-probe technique for measuring the thermal conductivity of liquids, Review of Scientific Instruments. 79 (2008) 064902. https://doi.org/10.1063/1.2937458.
[28] A. Grzechnik, G.H. Wolf, P.F. McMillan, Raman scattering study of SrTiO3 at high pressure, J. Raman Spectrosc. 28 (1997) 885–889. https://doi.org/10.1002/(SICI)1097-4555(199711)28:11<885::AID-JRS179>3.0.CO;2-Z.
[29] W.G. Nilsen, J.G. Skinner, Raman Spectrum of Potassium Tantalate, The Journal of Chemical Physics. 47 (1967) 1413–1418. https://doi.org/10.1063/1.1712096.

[30] Z. Zhang, K. Yuan, J. Zhu, X. Fan, J. Zhou, D. Tang, Thermal conductivity of $SrTiO_3$ under high-pressure, Appl. Phys. Lett. 120 (2022) 262201. https://doi.org/10.1063/5.0098353.
[31] W.-P. Hsieh, High-pressure thermal conductivity and compressional velocity of NaCl in B1 and B2 phase, Sci Rep. 11 (2021) 21321. https://doi.org/10.1038/s41598-021-00736-2.
[32] G.A. Samara, T. Sakudo, K. Yoshimitsu, Important Generalization Concerning the Role of Competing Forces in Displacive Phase Transitions, Phys. Rev. Lett. 35 (1975) 1767–1769. https://doi.org/10.1103/PhysRevLett.35.1767.
[33] D.A. Dalton, W.P. Hsieh, G.T. Hohensee, D.G. Cahill, A.F. Goncharov, Effect of mass disorder on the lattice thermal conductivity of MgO periclase under pressure, Scientific Reports. 3 (2013) 1–5. https://doi.org/10.1038/srep02400.
[34] B. Chen, W.P. Hsieh, D.G. Cahill, D.R. Trinkle, J. Li, Thermal conductivity of compressed H2O to 22 GPa: A test of the Leibfried-Schlömann equation, Physical Review B - Condensed Matter and Materials Physics. 83 (2011) 1–4. https://doi.org/10.1103/PhysRevB.83.132301.
[35] H. Bouafia, S. Hiadsi, B. Abidri, A. Akriche, L. Ghalouci, B. Sahli, Structural, elastic, electronic and thermodynamic properties of KTaO3 and NaTaO3: Ab initio investigations, Computational Materials Science. 75 (2013) 1–8. https://doi.org/10.1016/j.commatsci.2013.03.030.
[36] W.-P. Hsieh, A.F. Goncharov, S. Labrosse, N. Holtgrewe, S.S. Lobanov, I. Chuvashova, F. Deschamps, J.-F. Lin, Low thermal conductivity of iron-silicon alloys at Earth's core conditions with implications for the geodynamo, Nat Commun. 11 (2020) 3332. https://doi.org/10.1038/s41467-020-17106-7.
[37] W.-P. Hsieh, F. Deschamps, T. Okuchi, J.-F. Lin, Effects of iron on the lattice thermal conductivity of Earth's deep mantle and implications for mantle dynamics, Proc. Natl. Acad. Sci. U.S.A. 115 (2018) 4099–4104. https://doi.org/10.1073/pnas.1718557115.
[38] W. Hsieh, F. Deschamps, T. Okuchi, J. Lin, Reduced lattice thermal conductivity of Fe-bearing bridgmanite in Earth's deep mantle, J. Geophys. Res. Solid Earth. 122 (2017) 4900–4917. https://doi.org/10.1002/2017JB014339.
[39] E. Marzotto, W. Hsieh, T. Ishii, K. Chao, G.J. Golabek, M. Thielmann, E. Ohtani, Effect of Water on Lattice Thermal Conductivity of Ringwoodite and Its Implications for the Thermal Evolution of Descending Slabs, Geophys. Res. Lett. 47 (2020). https://doi.org/10.1029/2020GL087607.
[40] K. Chao, W. Hsieh, Thermal Conductivity Anomaly in $(Fe_{0.78}Mg_{0.22})CO_3$ Siderite Across Spin Transition of Iron, J. Geophys. Res. Solid Earth. 124 (2019) 1388–1396. https://doi.org/10.1029/2018JB017003.
[41] O.L. Anderson, A simplified method for calculating the debye temperature from elastic constants, Journal of Physics and Chemistry of Solids. 24 (1963) 909–917. https://doi.org/10.1016/0022-3697(63)90067-2.
[42] N.L. Vočadlo, G.D. Price, The Grüneisen parameter — computer calculations via lattice dynamics, Physics of the Earth and Planetary Interiors. 82 (1994) 261–270. https://doi.org/10.1016/0031-9201(94)90076-0.
[43] L. Feng, T. Shiga, J. Shiomi, Phonon transport in perovskite $SrTiO_3$ from first principles, Appl. Phys. Express. 8 (2015) 071501. https://doi.org/10.7567/APEX.8.071501.
[44] A. Boudali, M.D. Khodja, B. Amrani, D. Bourbie, K. Amara, A. Abada, First-principles study of structural, elastic, electronic, and thermal properties of SrTiO3 perovskite cubic, Physics Letters A. 373 (2009) 879–884. https://doi.org/10.1016/j.physleta.2008.12.017.
[45] S. Sarfraz, S.A. Aldaghfag, M.K. Butt, M. Yaseen, M. Zahid, A. Dahshan, Physical properties of KTaO3 compound for optoelectronic and thermoelectric applications: A DFT study, Materials Science in Semiconductor Processing. 148 (2022) 106811. https://doi.org/10.1016/j.mssp.2022.106811.

[46] A.V. Postnikov, T. Neumann, G. Borstel, M. Methfessel, Ferroelectric structure of KNbO 3 and KTaO 3 from first-principles calculations, Phys. Rev. B. 48 (1993) 5910–5918. https://doi.org/10.1103/PhysRevB.48.5910.
[47] N.K. Ravichandran, D. Broido, Phonon-Phonon Interactions in Strongly Bonded Solids: Selection Rules and Higher-Order Processes, Phys. Rev. X. 10 (2020) 021063. https://doi.org/10.1103/PhysRevX.10.021063.
[48] S. Lohrasbi, R. Hammer, W. Essl, G. Reiss, S. Defregger, W. Sanz, A Comprehensive Review on the Core Thermal Management Improvement Concepts in Power Electronics, IEEE Access. 8 (2020) 166880–166906. https://doi.org/10.1109/ACCESS.2020.3021946.
[49] T. Liu, X. Zhao, J. Li, Z. Liu, F. Liscio, S. Milita, B.C. Schroeder, O. Fenwick, Enhanced control of self-doping in halide perovskites for improved thermoelectric performance, Nat Commun. 10 (2019) 5750. https://doi.org/10.1038/s41467-019-13773-3.
[50] H. Ohta, Thermoelectrics based on strontium titanate, Materials Today. 10 (2007) 44–49. https://doi.org/10.1016/S1369-7021(07)70244-4.
[51] C.W. Li, J. Hong, A.F. May, D. Bansal, S. Chi, T. Hong, G. Ehlers, O. Delaire, Orbitally driven giant phonon anharmonicity in SnSe, Nature Phys. 11 (2015) 1063–1069. https://doi.org/10.1038/nphys3492.
[52] Y. Zhou, Z.-Y. Dong, W.-P. Hsieh, A.F. Goncharov, X.-J. Chen, Thermal conductivity of materials under pressure, Nat Rev Phys. 4 (2022) 319–335. https://doi.org/10.1038/s42254-022-00423-9.